

Machine Learning Coupled Multi-Scale Modeling for Redox Flow Batteries

Jie Bao,* Vijayakumar Murugesan, Carl Justin Kamp, Yuyan Shao, Litao Yan, and Wei Wang*

The framework of a multi-scale model that couples a deep neural network, a widely used machine learning approach, with a partial differential equation solver and provides understanding of the relationship between the pore-scale electrode structure reaction and device-scale electrochemical reaction uniformity within a redox flow battery is introduced. A deep neural network is trained and validated using 128 pore-scale simulations that provide a quantitative relationship between battery operating conditions and uniformity of the surface reaction for the pore-scale sample. Using the framework, information about surface reaction uniformity at the pore level to combined uniformity at the device level is upscaled. The information obtained using the framework and deep neural network against the experimental measurements is also validated. Based on the multi-scale model results, a time-varying optimization of electrolyte inlet velocity is established, which leads to a significant reduction in pump power consumption for targeted surface reaction uniformity but little reduction in electric power output for discharging. The multi-scale model coupled with the deep neural network approach establishes the critical link between the micro-structure of a flow-battery component and its performance at the device scale, thereby providing rationale for further operational or material optimization.

renewable resources, which is becoming one of the main challenges for modern grid management. Stationary energy storage with its ability to efficiently store and then release a large amount of energy on demand provides a viable solution to the challenge of managing energy generated from intermittent resources. By providing reliable renewable energy integration, balancing the mismatch between supply and demand, and improving overall grid reliability and efficiency, energy storage would become a critical component in grid modernization. As a promising energy-storage candidate for integration on the grid, the redox flow battery (RFB) is unique because it spatially separates the electrolyte and the electrode.^[1–4] This separation of the energy-bearing electrolyte and the power-generating stack makes the RFB a very safe technology and allows independent tuning of the energy and power ratio of the battery, which is a significant attribute for meeting various requirements for a diverse energy market. High capital cost is still a major challenge for the widespread deployment

of RFB systems, and Kim et al.^[5] indicates that the optimal operation for maximum system energy efficiency of RFB involves a tradeoff between electrochemical performance and pumping losses.

Currently, there are many types of RFBs, and each employs different redox couples. Examples of these couples include all-vanadium, Fe(II)/Fe(III) and V(IV)/V(V), Fe(II)/Fe(III) and Br₂/Br⁻, Ti-Mn/Ti-Mn, V-Mn-Ti/V-Mn-Ti, Ce(IV)/Ce(III), etc.^[6–8] However, the all-vanadium RFB (VRFB) is one of the most studied and developed flow-battery technologies and is most often used as a model system for various studies to provide better understanding and insight for the development of new chemistries and systems.^[6,9–12] Therefore, in our study, we used the VRFB technology for demonstrating the proposed model. In a VRFB, an electrolyte consisting of vanadium ions dissolved in a sulfuric acid (H₂SO₄) solution flows through porous electrodes. The V⁵⁺ (VO₂⁺) and V⁴⁺ (VO²⁺) ions are present in the positive electrolyte, while the V³⁺ and V²⁺ ions are present in the negative electrolyte.^[13]

In a more relevant case, a gas-diffusion electrode^[14–18] structure has been the subject of intensive studies for fuel cells over decades. These electrodes have a fundamentally different

1. Introduction

Driven by continuous reductions in production costs and the need to mitigate the carbon footprint associated with traditional fossil-fuel-based electricity generation, the amount of energy produced from renewable resources such as solar and wind is steadily increasing. The caveat to this situation, however, is the intermittent and fluctuating nature of energy produced from

Dr. J. Bao, Dr. V. Murugesan, Dr. Y. Shao, Dr. L. Yan, Dr. W. Wang
Pacific Northwest National Laboratory
Richland, WA 99352, USA

E-mail: jie.bao@pnnl.gov; wei.wang@pnnl.gov

Dr. C. J. Kamp
Massachusetts Institute of Technology
Boston, MA 02139, USA

Dr. C. J. Kamp
Kymanetics, Inc.
Boston, MA 02152, USA

 The ORCID identification number(s) for the author(s) of this article can be found under <https://doi.org/10.1002/adts.201900167>

DOI: 10.1002/adts.201900167

working mechanism in that the reactants are liquids in true RFBs and gases in fuel cells. Graphite-felt electrodes used in RFBs typically are catalyst-free, so no triple-phase boundary^[19–21] is present. As a result, unlike gaseous reactants in fuel cells, the reactant ions carried in the liquid electrolyte in a RFB usually cannot access nanoscale pores. The redox reactions proceed mainly at the surfaces of the electrodes. As such, while the dominant energy loss in a gas-diffusion electrode structure is the imperfect catalysis of the redox reactions, losses due to mass transport and electron conduction are not as significant. Mass transport is a much more prominent limitation for redox flow batteries using liquid electrolytes as reactants; however, studies focused on simulating this mechanism have been lacking.

Simulation studies on components and performance have been an important area in RFB research, providing theoretical and systematic understanding of the technology.^[22–25] However, a viable model that connects the RFB component micro-structure with its device-scale performance has not been developed. For example, reaction distribution at the device scale has been studied using both numerical modeling and experimental measurements.^[6,26–28] Additionally, Qiu et al.^[13,29] performed pore-scale modeling that coupled species/charge/fluid transport and simulated reaction distributions on the electrode surface at 3D pore scales for several given operating conditions. Their results show that an electrode with high porosity leads to larger variations in the reaction distribution. However, the manner in which the reaction distribution at the pore scale impacts device-scale performance still has not been clearly elucidated.

A direct pore-scale simulation usually requires the use of a very high-resolution mesh, which may be at the micron level or even smaller. This requirement leads to millions to billions of mesh elements for a small size sample. Because of the large number of mesh elements required, a pore-scale simulation is computationally demanding and expensive. Meanwhile, the device-scale model needs pore-scale information for many operating conditions, such as combinations of different flow rates, current densities, and electrolyte concentrations. Implementation of a pore-scale simulation for all conditions at the device scale is difficult due to the computational cost. However, an efficient way to overcome this limitation would be to use pore-scale simulations for only a limited number of representative operating conditions and then build a machine learning (ML) architecture trained by the limited number of direct simulation results. With recent developments in hardware and software, ML has been applied in various areas, especially for image and natural language recognition.^[30,31] For battery-related science and engineering, ML applications are still very limited although a few ideas have been proposed.^[32–35]

Additionally, it is very challenging to quantitatively determine the relationship between micro-scale phenomena and device-scale performance. A multi-scale framework is a viable approach for indirectly passing information to a device-scale model. For example, Bao et al.^[36] and Pan et al.^[37] introduced an upscaling approach that connects the pore structure of the cathode and device-scale discharging performance of an LiO₂ battery and used the approach to optimize the design of the cathode pore structure. In our study, we applied a multi-scale framework coupled with ML to connect pore-scale modeling to device-scale estimation for

a flow battery and used the approach to optimize the inlet flow rate.

The pore-scale model is the foundation of the multi-scale framework so the high-resolution pore-scale geometry of the electrode plays an important role in laying the foundation for creating a high-fidelity model. In our study, the electrode is composed of carbon fibers that form an electrically conductive fibrous network. High-resolution X-ray computed tomography can be used to accurately measure and digitally reconstruct the 3D pore-scale structure of an electrode.^[38] Typically, X-rays absorb less in lighter elements than in heavier elements, which can thus make scanning a full carbon sample somewhat difficult. However, several specific techniques can be used to improve the contrast in samples of lighter elements. These techniques include low-energy X-ray filtration (typically using tin, aluminum, or copper), highly stable reduced sample sizes with custom sample holders, X-ray focusing/beam attenuation, various correction algorithms in the reconstruction software, and optimized X-ray conditions.

For this study, we used an XTEK 225 micro-computed tomography (CT) system at the Harvard University Center for Nanoscale Systems to analyze the electrode samples. The XTEK 225 system is a multisource (tungsten was used in this case) instrument with a 16 in. × 16 in. Perkin Elmer detector that used geometric magnification capable of ≈1 μm resolution. Scanned data were reconstructed with the CT 3D Pro software from Nikon, and we used VGStudio Max and Avizo for the imaging segmentation analyses.

The pore-scale fluid dynamics model with electrochemical reactions, the deep neural network (DNN), the multi-scale framework, and the experimental configurations are described in Section 3. Application of the proposed model on an X-ray scanned electrode sample, model validation against experimental measurements, and results are presented in Section 4. The proposed model provides the capability to optimize electrolyte inlet flow rate, which can significantly reduce the power consumed for pumping the electrolyte while not impacting the electric power output for discharging, thus potentially improving the VRFB system efficiency by ≈6%.

2. Methodology

As mentioned previously, redox flow batteries and particularly VRFBs, are promising candidates for stationary energy storage because of their high safety, decoupled energy and power, and modular design. Our VRFB setup (see Figure 1) mainly consists of current collectors for both positive and negative electrodes (gray blocks), porous negative (orange block) and positive (green block) electrodes, ion-exchange membrane (blue block), and electrolyte storage tanks (orange and green cylinders). The orange lines and arrows show the negative electrolyte flow direction, and the green lines and arrows show the positive electrolyte flow direction. The purple solid line with an arrow shows the direction of electron movement during discharge, and the red dash line with an arrow shows the direction of electron movement during charge.

During discharge, in the positive electrode, V⁵⁺ converts to V⁴⁺ through the electrochemical reaction VO₂⁺ + 2H⁺ + e⁻ → VO²⁺ + H₂O, while in the negative electrode, V²⁺ converts to

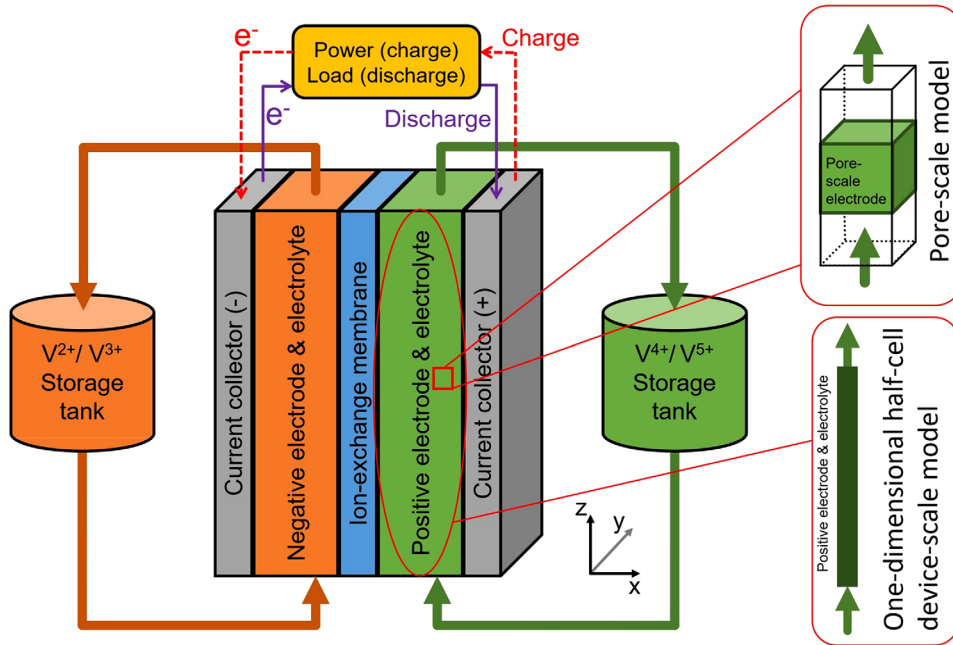


Figure 1. Flow-battery setup. The inserts are sketch of the pore-scale model and 1D half-cell device-scale model setups.

V^{3+} through the electrochemical reaction $V^{2+} \rightarrow V^{3+} + e^-$. During charge, all the reactions are reversed. Because the reactions in positive and negative electrodes share the very similar mechanisms, we focused on the positive electrode to demonstrate the proposed ML-coupled multi-scale modeling approach.

2.1. Pore-Scale Fluid Dynamics Model

The pore-scale model focuses on mass transport in the porous electrode with detailed pore structures. The insert in Figure 1 shows the pore-scale modeling domain, in which the green block represents a pore structure of the porous electrode, the void space represents the buffer zone to reduce inlet/outlet boundary effects, and the green arrows represent the electrolyte flow direction. For pore-scale fluid transport, the lattice Boltzmann equation (LBE) model has been applied for modeling VRFBs and other battery systems at the pore scale^[13,29,36,37] because of its simple wall boundary treatment method and high parallel computational efficiency.^[39–42] The LBE model is derived from the continuum Boltzmann Bhatnagar–Gross–Krook (BGK) equation.^[43] The evolution equation can be discretized in momentum, time, and space dimensions as shown in Equation (1)

$$f_\alpha(\vec{x} + \vec{e}_\alpha \Delta t, t + \Delta t) = f_\alpha(\vec{x}, t) - \frac{1}{\tau} [f_\alpha(\vec{x}, t) - f_\alpha^{eq}(\vec{x}, t)] \quad (1)$$

where f_α is the particle distribution function along the α -th-direction, which describes the probability of a particle moving along a given direction. α represents the discretized directions. For 2D problems, there are nine directions, and for 3D problems, there can be 13, 19, or 27 directions.^[44–46] \vec{x} represents the location in space, t is time, Δt is a short time step interval, and \vec{e}_α is lattice velocity vector. $\tau = \frac{v}{c_s^2 \Delta t} + 0.5$ is the relaxation time, where

v is the viscosity and $c_s = \frac{\Delta x}{\sqrt{3} \Delta t}$ is the speed of sound in the LBE model. f_α^{eq} is the equilibrium particle distribution function, which can be expressed as

$$f_\alpha^{eq} = \rho w_\alpha \left[1 + \frac{3}{c^2} \vec{e}_\alpha \cdot \vec{u} + \frac{9}{2c^4} (\vec{e}_\alpha \cdot \vec{u})^2 - \frac{3}{2c^2} \vec{u} \cdot \vec{u} \right] \quad (2)$$

where w_α is the weight factor, $c = \frac{\Delta x}{\Delta t}$ is the lattice speed, $\rho = \sum_{\alpha=0}^N f_\alpha$ is fluid density, and $\vec{u} = \frac{1}{\rho} \sum_{\alpha=0}^N f_\alpha \vec{e}_\alpha$ is velocity. Equation (1) can be applied on all the fluid lattice. For a fluid lattice at \vec{x} whose neighbor $\vec{x} + \vec{e}_\alpha \Delta t$ is a solid lattice, the half-way bounce-back method is used for the boundary condition.^[44]

2.2. Pore-Scale Electrochemical Reaction Model

The evolution of V^{4+} and V^{5+} concentration in the positive electrode is governed by Equations (3) and (4)

$$\frac{\partial c_4}{\partial t} + \vec{u} \nabla c_4 = D_4 \nabla^2 c_4 + \frac{aj}{nF} \quad (3)$$

$$\frac{\partial c_5}{\partial t} + \vec{u} \nabla c_5 = D_5 \nabla^2 c_5 - \frac{aj}{nF} \quad (4)$$

Here, c_4 and c_5 are the concentrations of V^{4+} and V^{5+} , respectively; j is the faradaic current density; and a is local surface-to-volume ratio of the positive electrode. In LBM-scheme, pore-scale simulations, a has value of local surface-to-volume only in the fluid lattice next to solid grids, otherwise, it is zero. $n = 1$ is the number of electrons involved in the reaction: $VO_2^+ + 2H^+ + e^- \rightarrow VO^{2+} + H_2O$. F is the Faraday constant. D_4 and D_5 are the diffusion coefficients of V^{4+} and V^{5+} , respectively, both of which are

$3.9 \times 10^{-10} \text{ m}^2 \text{ s}^{-1}$.^[12,13,22,23,29] The faradaic current density j is assumed to follow a Tafel kinetics relationship

$$j = nFk(c_4c_5)^{1-\beta} \exp\left(-\frac{\beta nF\eta}{RT}\right), \quad (5)$$

where k is the kinetic rate, β is the charge transfer coefficient, η is the Tafel overpotential, R is the gas constant, and T is the temperature. The total current I is distributed on all the pore-scale electrode surface, and can be related to the Faradaic current density j by Equation (6)

$$I = \sum_V a\Delta x^3 j \quad (6)$$

where \sum_V stands for summation over all the pore volume and $a\Delta x^3$ is the calculation of local pore-scale surface area. Combining Equations (5) and (6) yields

$$\eta = -\frac{RT}{\beta nF} \ln\left(\frac{I}{\sum_V a\Delta x^3 nFk(c_4c_5)^{1-\beta}}\right). \quad (7)$$

2.3. Device-Scale Electrochemical Reaction Model

In this study, we used a 1D half-cell model (positive electrode) to simulate device-scale mass transport and electrochemical reactions in the positive electrode (see insert in Figure 1). The governing equations for device-scale modeling are the same as the ones for pore-scale modeling (Equations (3)–(7)) for the overpotential (η) and Faradaic current density (j). Equation (8) is used to calculate the device-scale open circuit voltage (E_{ocv}) for the VRFB.^[47]

$$E_{\text{ocv}} = E_p^0 - E_n^0 + \frac{RT}{F} \ln\left(\frac{\bar{c}_2\bar{c}_5(\bar{c}_{H_p})^3}{\bar{c}_3\bar{c}_4\bar{c}_{H_2O_p}\bar{c}_{H_n}}\right) \quad (8)$$

E_p^0 and E_n^0 are the standard reaction potentials of the positive and negative electrode half reactions, respectively. The terms \bar{c}_4 and \bar{c}_5 are the average concentrations of V^{4+} and V^{5+} in the positive electrode, and \bar{c}_2 and \bar{c}_3 are the average concentrations of V^{2+} and V^{3+} in the negative electrode. The terms \bar{c}_{H_p} and \bar{c}_{H_n} are the averaged concentrations of protons in the positive and negative electrodes, respectively. The term $\bar{c}_{H_2O_p}$ is the averaged concentration of water in the positive electrode. All of the averaged concentrations are estimated according to the state of charge (SOC) and, for discharging, are calculated using Equation (9).^[13,29]

$$\text{SOC} = \frac{\bar{c}_2}{\bar{c}_n^0} = \frac{\bar{c}_5}{\bar{c}_p^0},$$

$$\bar{c}_2 = \bar{c}_n^0 \times \text{SOC},$$

$$\bar{c}_3 = \bar{c}_n^0 \times (1 - \text{SOC}),$$

$$\bar{c}_4 = \bar{c}_p^0 \times (1 - \text{SOC}),$$

$$\bar{c}_5 = \bar{c}_p^0 \times \text{SOC},$$

$$\bar{c}_{H_n} = \bar{c}_{H_n}^0 - \bar{c}_n^0 \times \text{SOC},$$

$$\bar{c}_{H_p} = \bar{c}_{H_p}^0 - \bar{c}_p^0 \times \text{SOC},$$

$$\bar{c}_{H_2O_p} = \bar{c}_{H_2O_p}^0 + \bar{c}_p^0 \times \text{SOC} \quad (9)$$

The terms \bar{c}_p^0 and \bar{c}_n^0 are the total vanadium concentrations in the positive and negative electrodes. The terms $\bar{c}_{H_p}^0$ and $\bar{c}_{H_n}^0$ are the initial proton concentration in the positive and negative electrodes. $\bar{c}_{H_2O_p}^0$ is the initial water concentration in the positive electrode.

Equation (10) is used to estimate the ohmic loss of the VRFB.^[47]

$$\eta_{\text{ohm}} = \left(\frac{w_m}{\sigma_m} + \frac{2w_e}{\sigma_e \epsilon^{1.5}} + \frac{2w_c}{\sigma_c}\right) J \quad (10)$$

where w_m , w_e , and w_c are the thickness (x direction in Figure 1) of the membrane, electrode, and current collector, σ_m , σ_e , and σ_c are the conductivity, ϵ is the electrode porosity, and J is the discharge current density.

The overall voltage of the investigated VRFB is calculated using Equation (11).

$$E = E_{\text{ocv}} + \eta - \eta_{\text{ohm}} - \eta_n \quad (11)$$

where η is the overpotential in the positive electrode directly derived from the 1D half-cell model (Equations (3)–(7)), and η_n is the overpotential in the negative electrode. Because the negative electrode is not directly modeled in this study, we used an averaged value of 0.05 V for Equation (11). All the operating parameters and property values used in this study are listed in Table 1.

2.4. Deep Neural Networks

2.4.1. Sampling Method

The concentration distributions and surface reaction rate distribution can be determined by solving Equations (1)–(7), with given total current on a pore-scale sample, flow speed, and inlet V^{5+} concentration. Considering a flow battery can work under a variety of operating conditions, which means there are infinite combinations of flow speed, electric current, and inlet concentration, we can only simulate a limited number of operating conditions. The conditions that are not directly simulated can be estimated by the DNN. Picking the battery operating conditions is critical when building an efficient and accurate DNN. Therefore, we used the quasi-Monte Carlo (QMC) sampling method to select cases for simulation. QMC methods have become increasingly popular over the last two decades because of their faster convergence speeds and effective sampling of high-dimensional parametric space without clumping and gaps.^[48,49] In our study, 128 QMC samples were generated from existing scrambled Sobol sequences^[50,51] that ranged from 0 to 1 and were scaled to the actual input parameter ranges listed in Table 2 for inlet flow velocity, electric current density, and inlet concentration.

Table 1. Operating parameters and properties used in the modeling.

Description	Symbol	Value	Units
Diffusion coefficients of V ⁴⁺	D_4	3.9×10^{-10} [6]	m^2s^{-1}
Diffusion coefficients of V ⁵⁺	D_5	3.9×10^{-10} [6]	m^2s^{-1}
Current	I	0.75	A
Current density	J	750	A m^{-2}
Standard reaction potentials of the positive electrode half reactions	E_p^0	1.004[6]	V
Standard reaction potentials of the negative electrode half reactions	E_n^0	-0.255[6]	V
Thickness of the membrane (x direction in Figure 1)	w_m	1.25×10^{-4}	m
Thickness of the electrode (x direction in Figure 1)	w_e	0.003	m
Thickness of the current collector (x direction in Figure 1)	w_c	0.015	m
Conductivity of the membrane	σ_m	$10^{[47]}$	S m^{-1}
Conductivity of the electrode	σ_e	1000[6]	S m^{-1}
Conductivity of the current collector	σ_c	5000[22]	S m^{-1}
Averaged overpotential in the negative electrode	η_n	0.05	V
Initial vanadium concentration in the positive electrode	\bar{c}_p^0	1500	mol m^{-3}
Initial vanadium concentration in the negative electrode	\bar{c}_n^0	1500	mol m^{-3}
Initial proton concentration in the positive electrode	$\bar{c}_{H_p}^0$	7000	mol m^{-3}
Initial proton concentration in the negative electrode	$\bar{c}_{H_n}^0$	7000	mol m^{-3}
Initial water concentration in the positive electrode	$\bar{c}_{H_2O_p}^0$	4600	mol m^{-3}
Transfer coefficient	β	0.5	—
Standard reaction rate constant	k	6.8×10^{-7} [6]	m s^{-1}
Number of electrons involved in the reaction	n	1	—
Surface-to-volume ratio of the electrode	a	3.48×10^4	m^{-1}
Porosity of the electrode	ϵ	0.814	—
Viscosity of the electrolyte	ν	1×10^{-6} [29]	m^2s^{-1}
Density of the electrolyte	ρ	1000[29]	kg m^{-3}
Operating temperature	T	298	K

Table 2. Input parameters and their ranges.

Input parameters	Range
Inlet velocity [m s^{-1}]	5.5×10^{-5} to 5.5×10^{-3}
Current density [A m^{-3}]	1.7×10^5 to 3.5×10^6
Inlet concentration [mol m^{-3}]	100–2000

2.4.2. Deep Neural Networks

DNN is one of the widely used deep-learning architectures, and deep learning is part of a broader family of ML methods based on the layers used in artificial neural networks.^[52] The upper part of **Figure 2** (within the box enclosed in the dashed blue border) shows the DNN scheme used in this study.

The input layer includes the three input parameters introduced in Section 3.4.1. The output layer includes the normalized standard deviation of the surface reaction rate, σ_r , and the full cumulative distribution function (CDF) of the surface reaction rate. The CDF is the integral of the probability distribution function (PDF), so the CDF and PDF are equivalent. However, because the CDF is a monotonic function, it is more efficient for train-

ing the DNN. Neural nodes in the DNN, delineated a_{ij} , connect the input layer and the output layer through several hidden layers. In this study, we used four hidden layers, with 64, 400, 400, and 400 neural nodes for each hidden layer. Generally, there is no precise rule for choosing the number of hidden layers and neural nodes. In this study, the number of layers and neural nodes were adjusted to approximately balance the training convergence speed and the validation set prediction accuracy. The insert in the red box in Figure 2 shows the structure of one neural node. Generally, in each neural node, the inputs multiply the weights, w_{ij} ; and add with the biases, b_i ; and then are modified by an activation function. In this study, a rectifier function is used as the activation function for all of the hidden layers. Each successive layer uses the input from the previous layer as input.^[30] In this study, the available data (128 samples as mentioned in Section 3.4.1) are divided into two parts—100 samples for training and 28 samples for testing. The DNN training process searches for values for all of the weights and biases to minimize the error between the true values and the DNN predictions. The testing set is used to evaluate the performance of the trained DNN for the new data that is blind to the DNN training procedure. In this study, we used the ML package Tensorflow^[53] to construct and train the DNN.

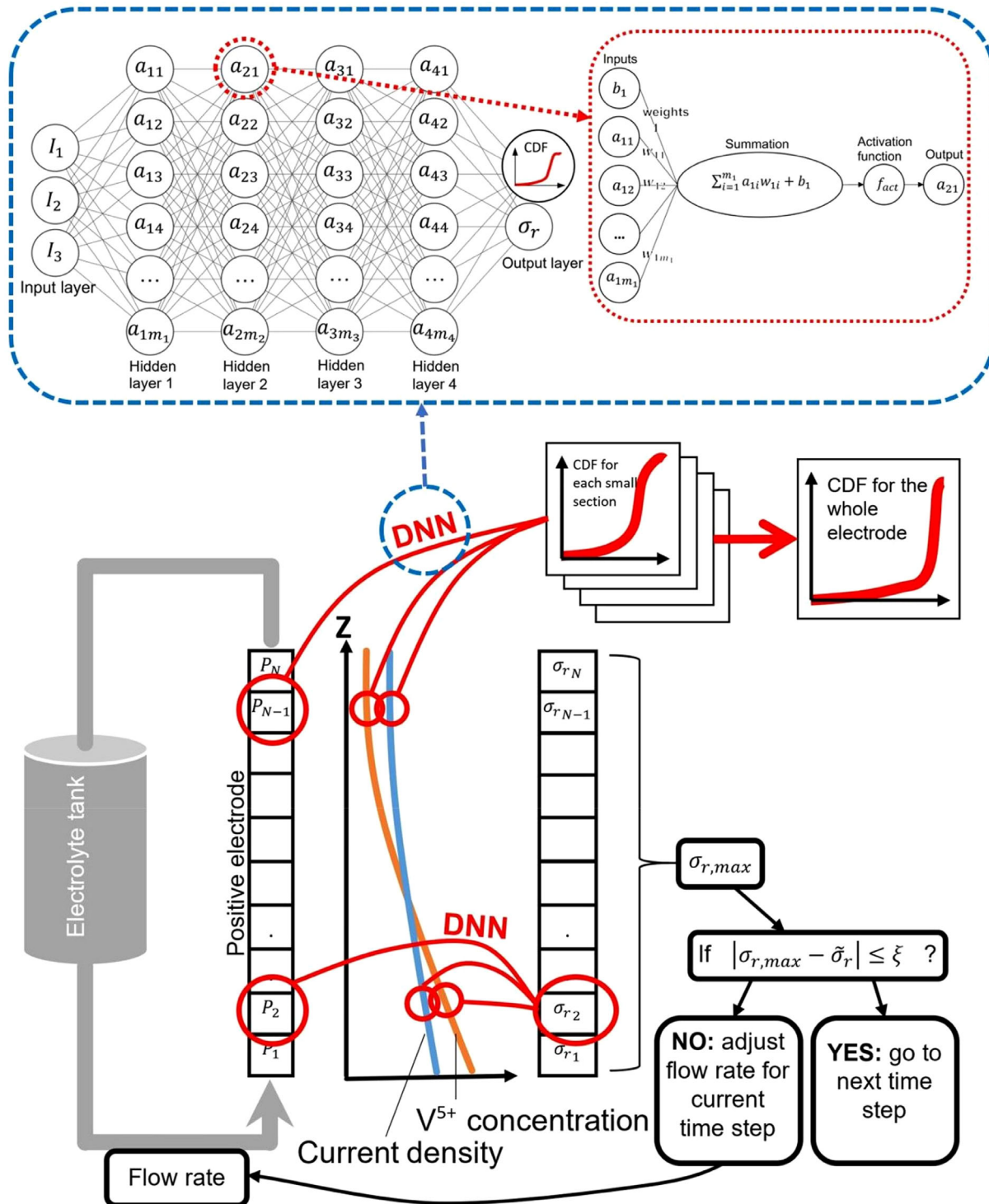


Figure 2. Graphical representation of the 1D device-scale simulation and multi-scale model flow chart. The insert within the box enclosed by the dashed blue border is the DNN scheme used for learning the relationship between flow-battery operating conditions and surface reaction uniformity.

2.5. Multi-Scale Model for the Device Scale

In this study, we used a simplified 1D model for the device-scale flow battery as discussed in Section 3.3 and shown in Figures 1 and 2 (lower part). With a given total charge current and total elec-

trolyte volume, V^{4+} and V^{5+} concentration evolution along the flow direction can be solved using Equations (3)–(7). The whole device-scale, 1D, half-cell modeling domain can be discretized into many small sections that are marked $P_1, P_2, P_3 \dots P_{N-1}, P_N$ in Figure 2. Each section has its local current density and average

concentration, which are shown as the orange and blue curves in Figure 2. The inlet flow speed should be the same for all the small sections because the model is 1D. Using the local current density, average concentration, and flow inlet speed as the input parameters, the DNN can estimate the normalized standard deviation of surface reaction rate, σ_r , for each small section (noted as $\sigma_{r1} \dots \sigma_{rN}$ in Figure 2). Then, by combining the standard deviations ($\sigma_{r1} \dots \sigma_{rN}$) for all the small sections, the overall standard deviation, σ_r , for the whole device-scale model can be predicted by following the combined variance rule

$$\sigma_r c^2 = \frac{n_1 \sigma_{r1}^2 + n_2 \sigma_{r2}^2 + n_1 (\bar{y}_1 - \bar{y}_c)^2 + n_2 (\bar{y}_2 - \bar{y}_c)^2}{n_1 + n_2} \quad (12)$$

$$\sigma_{r,max}^2 = \max(\sigma_{r1}^2, \sigma_{r2}^2, \sigma_{rc}^2) \quad (13)$$

where n_1 and n_2 are the numbers of the two combined data. The terms \bar{y}_1 and \bar{y}_2 are the mean of the two combined data points, respectively. The function \max is used to find the maximum value of each element. This function avoids the extreme situation in which the reaction occurs only in a small region near the inlet, and the reaction rate is zero in the rest of the electrode, which can make the combined variance, $\sigma_r c^2$, still very small but definitely would not be expected in the device. The term \bar{y}_c is the combined mean, which is calculated using Equation (14).

$$\bar{y}_c = \frac{n_1 \bar{y}_1 + n_2 \bar{y}_2}{n_1 + n_2} \quad (14)$$

Figure 2 shows the developed multi-scale modeling framework (red circle and arrows). The model estimated σ_r can be compared with the targeted uniformity of the surface reaction rate $\tilde{\sigma}_r$. If the estimated $|\sigma_{r,max} - \tilde{\sigma}_r|$ is smaller than a user-defined tolerance, it means the uniformity of the surface reaction rate meets the expectation. If this condition is satisfied, the routine then progresses to the next time step. If it does not meet the expectation, the electrolyte flow rate should be adjusted, and this multi-scale modeling framework should be repeated to get a new $\sigma_{r,max}$ until $|\sigma_{r,max} - \tilde{\sigma}_r| \leq \xi$. This optimization routine is repeated for every time step, leading to the optimized time-varying flow rate. Meanwhile, the DNN also predicts the CDF for each small section. The average of the CDFs for the sections represents the overall surface reaction distribution for the whole electrode. This average CDF can provide researchers a more direct view of the surface reaction rate distribution for the whole electrode.

2.6. Flow-Battery Experiment Test

To validate the proposed model, corresponding experiments were undertaken. The initial electrolytes were prepared by dissolving 1.5 M VOSO₄ (Aldrich, 99%) in 3.5 M H₂SO₄ solution (Aldrich, 96–98%). Graphite felt was used for both the negative and positive electrodes with active areas of 10 cm² (5 cm long × 2 cm wide). The electrodes were 3 mm thick. Figure 3a shows the scanning electron microscope image of the electrode sample. Figure 3b shows the reconstructed 3D CT data after imaging segmentation analyses by VGStudio Max and Avizo.

Based on the reconstructed 3D CT data, the porosity of the sample is 0.814, the surface-to-volume ratio is 3.48 × 10⁴ m⁻¹, the mean fiber diameter is 12 μm, and the median pore diameter is 49 μm. The graphite felt manufacturer reported testing data show that the mean fiber diameter is about 10 μm, and the surface area (based on Brunauer–Emmett–Teller theory) is 0.4–0.5 m² g⁻¹, which is approximately equivalent to a surface-to-volume ratio of 4 × 10⁴ to 5 × 10⁴ m⁻¹. The reconstructed 3D CT data can fairly well match the manufacturer's data, although with some bias that may be caused by the CT resolution limits. Because the simulation geometry used in this study is based on the reconstructed 3D CT data, the pore-structure geometry parameters (porosity and surface-to-volume ratio) from the 3D CT data were used. Nafion 115 was used as the membrane. Electrolytes stored in two separate glass reservoirs (80 mL each) were circulated through the flow battery at a flow rate of 20 mL min⁻¹ by a peristaltic pump. The electrochemical performance of the flow cell was recorded using a potentiostat/galvanostat (Arbin Instrument, USA) within a fixed voltage range between 0.8 and 1.6 V under a constant current density of 75 mA cm⁻². The SOC for the tested battery charged to 1.6 V is about 0.75. Cyclic voltammetry study has been conducted and reported in previous studies.^[54] Figure 3c shows the battery cycle performance. A decrease in charge/discharge capacity was observed over the first 130 cycles. After that, the capacity of ≈1.5 Ah could be maintained for 70 more cycles. Because the proposed model does not consider cross contamination in VRFB, it cannot estimate the capacity decrease with charge–discharge cycles. Therefore, only the discharge data measured in the first cycle was used to validate the proposed model, which is discussed in Section 4.3. Figure 3d shows the evolution of columbic efficiency (CE) and energy efficiency (EE) during cycling for the investigated battery. The CE was maintained at 98%, and EE were maintained at 86% for 200 cycles.

2.7. Data Availability

The data that support the findings of this study are available from the corresponding author upon reasonable request.

3. Results

3.1. Pore-Scale Simulation Results

The pore-scale simulation geometry was generated from the reconstructed 3D CT data, with dimensions of 0.8 × 0.8 × 1.0 mm for the x , y , and z directions, respectively (see Figure 4a). The simulation mesh resolution is 4 μm. Flow is along the z direction, and a buffer zone is added for flow-field development. The four side boundaries are periodic; the bottom boundary is inlet with a given flow speed, and the upper boundary is a pressure boundary with a fixed reference pressure. Figure 4a shows streamlines of the fluid flow through the pore-scale geometry. The inlet velocity is 0.0013 m s⁻¹. Figure 4b shows the scatter-point cloud of the surface reaction rate, with an inlet concentration of V⁴⁺ = 1500 mol m⁻³ and an electric current density of 2.7 × 10⁵ A m⁻³. There is an obvious low reaction rate area in this sample (the blue area in Figure 4b). After statistical analysis

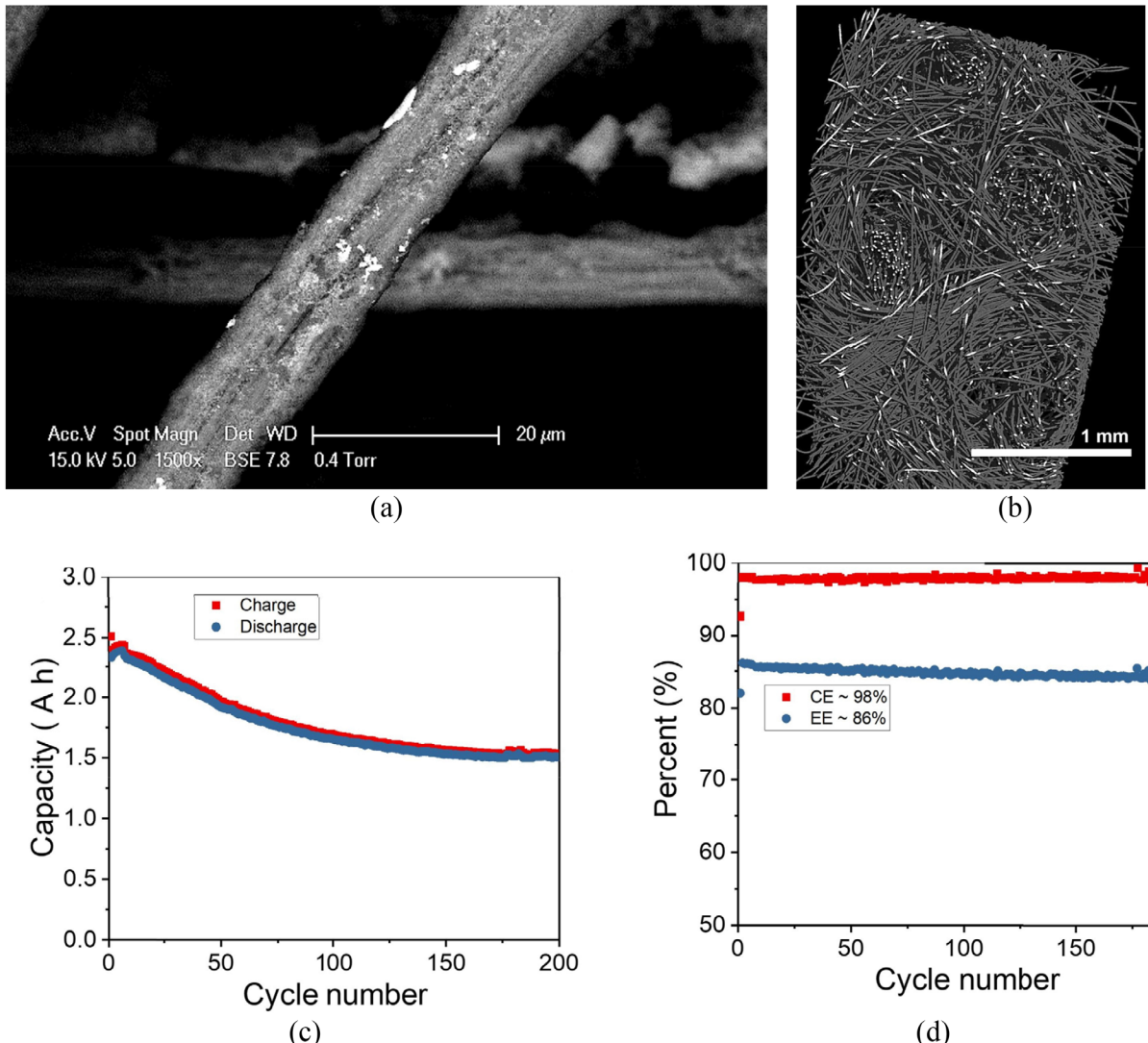


Figure 3. a) Scanning electron microscope image of the electrode sample; b) reconstructed 3D CT data after imaging segmentation analyses; c) capacity changes with cycles; and d) columbic efficiency and energy efficiency changes with cycles.

of the pore-scale simulation results for this specific sample, Figure 4c shows the histogram and the CDF of the surface reaction rate. The CDF curve transits from 0 to 1. If the transition is very sharp, the surface reaction rate is very uniform. Otherwise, the smooth transition in CDF means the surface reaction rate varies significantly at different locations on the electrode surface. The mean surface reaction rate, $\bar{\gamma}$, is $7.7 \times 10^{-3} \text{ mol m}^{-2} \text{ s}^{-1}$, and the standard deviation of the surface reaction rate, σ , is $7.9 \times 10^{-4} \text{ mol m}^{-2} \text{ s}^{-1}$, therefore, the normalized standard deviation of surface reaction rate, $\sigma_r = \sigma/\bar{\gamma}$, is $\approx 10\%$. The pore-scale simulation was implemented in the massively parallel computational fluid dynamics (CFD) program, ParaFlow. The pore-scale simulation ran on Pacific Northwest National Laboratory's Institutional Computing (PIC) High-Performance Computing (HPC) Cluster Constance with each simulation running on 96 cores. In terms of computing time, the flow transport simulation cost was ≈ 15 h, and the electrochemical reaction model cost was ≈ 4 h.

3.2. DNN and Response Surface

In this study, we assumed inlet velocity, inlet concentration, and electric current density are the three input parameters that affect the uniformity of the surface reaction rate. We used the QMC method to sample 128 simulation cases, which represents 128 different battery operating conditions as shown in Figure 5a. The ranges of the three input parameters are listed in Table 2. By running the pore-scale simulation described in Section 4.1 for the sampled 128 simulation cases, the normalized standard deviation of surface reaction rate, σ_r , and the CDF for the 128 battery operating conditions can be calculated.

Figure 5b shows the boxplots^[55,56] representing qualitative relationships among the input parameters and the output parameter σ_r based on the pore-scale simulation results. As the inlet velocity or concentration increases, σ_r decreases, which means the surface reaction rate is more uniform and is favorable. As the current density increases, σ_r increases as well, which means

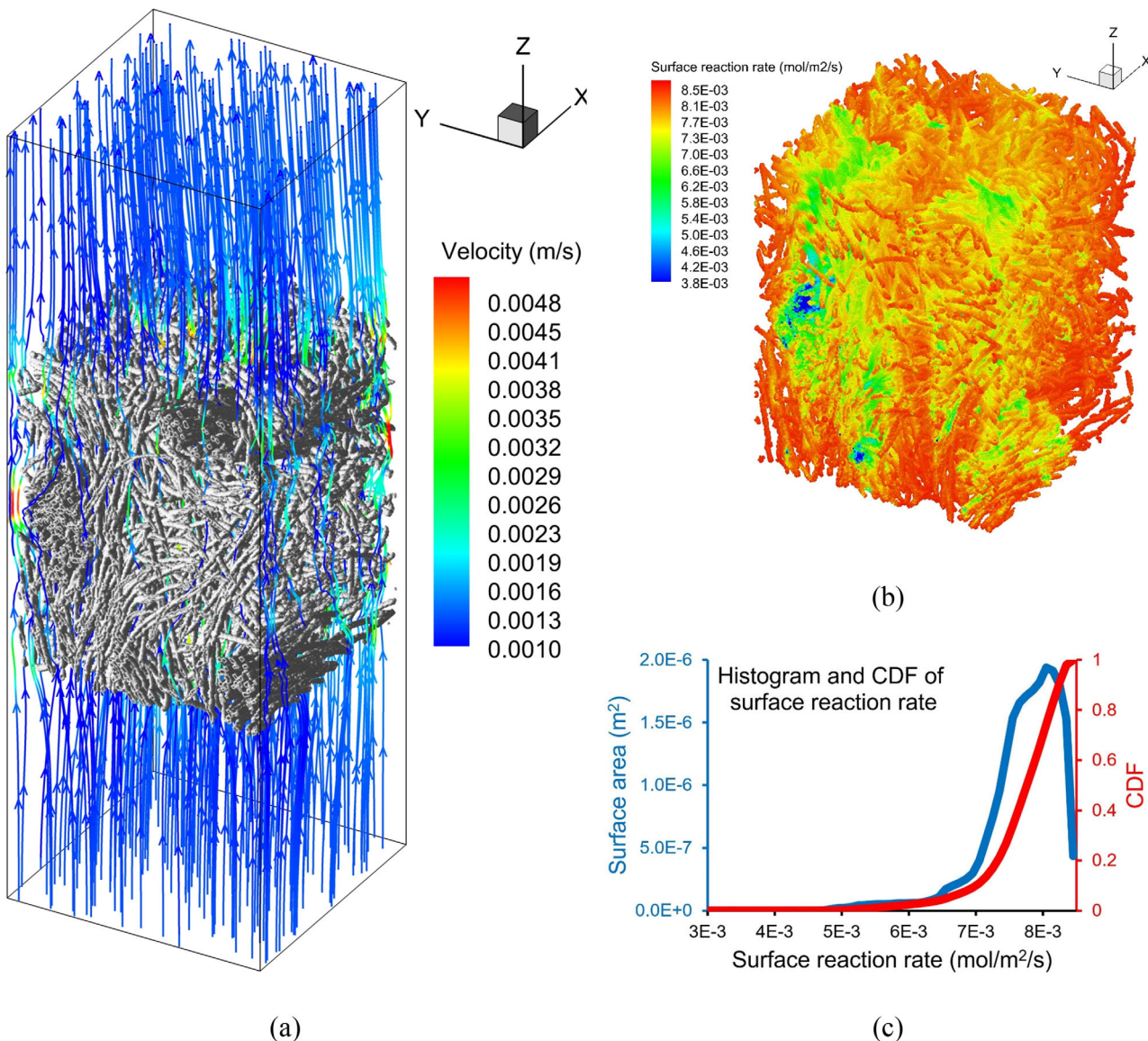


Figure 4. Pore-scale simulation demonstration. a) Pore-scale sample and streamlines; b) scatter-point cloud showing the surface reaction rate; and c) histogram and CDF of surface reaction rate.

the surface reaction rate is less uniform. For comparing the accuracy of the DNN prediction, we used a traditional regression model, multivariate adaptive regression splines (MARS),^[57] to predict the desired outputs with the same training and testing data sets. Figure 5c shows the “one-one” plot to compare the DNN and MARS predicted normalized standard deviations, σ_r , against the true value from simulations for the testing data set. Generally, both MARS and DNN can match the true data; however, quantitatively, the root mean square error (RMSE) for MARS is $\approx 9 \times 10^{-3}$, while for DNN, it is $\approx 1.8 \times 10^{-3}$. Figure 5d shows the “one-one” plot to compare the DNN and MARS predicted CDFs against the true CDFs from simulations for the testing data set. It is obvious that DNN can match the true data fairly well, but MARS shows relatively large deviations from the true data. Quantitatively, the RMSE for the MARS predicted CDFs are $\approx 5 \times 10^{-4}$,

while for DNN, it is $\approx 1.5 \times 10^{-5}$. MARS predicted CDFs are not usable because of the large RMSEs, which is on the same order of magnitude of the median value of the CDFs. Therefore, in this study, the DNN provided more reliable predictions than MARS. As mentioned in Section 4.1, each direct simulation costs ≈ 20 h running on 96 cores on HPC cluster, while the trained DNN can provide an estimate in <0.01 s.

With the validated DNN, σ_r can be estimated for any battery operating condition. Figure 5e shows slices of the response surface of σ_r . The three axes represent the three input parameters. The colors in Figure 5e represent the values of σ_r . The red area means σ_r is equal or greater than 50%. The green area means σ_r is between 10% and 50%. The light blue area means σ_r is between 5% and 10%. In empty areas, σ_r is smaller than 5%.

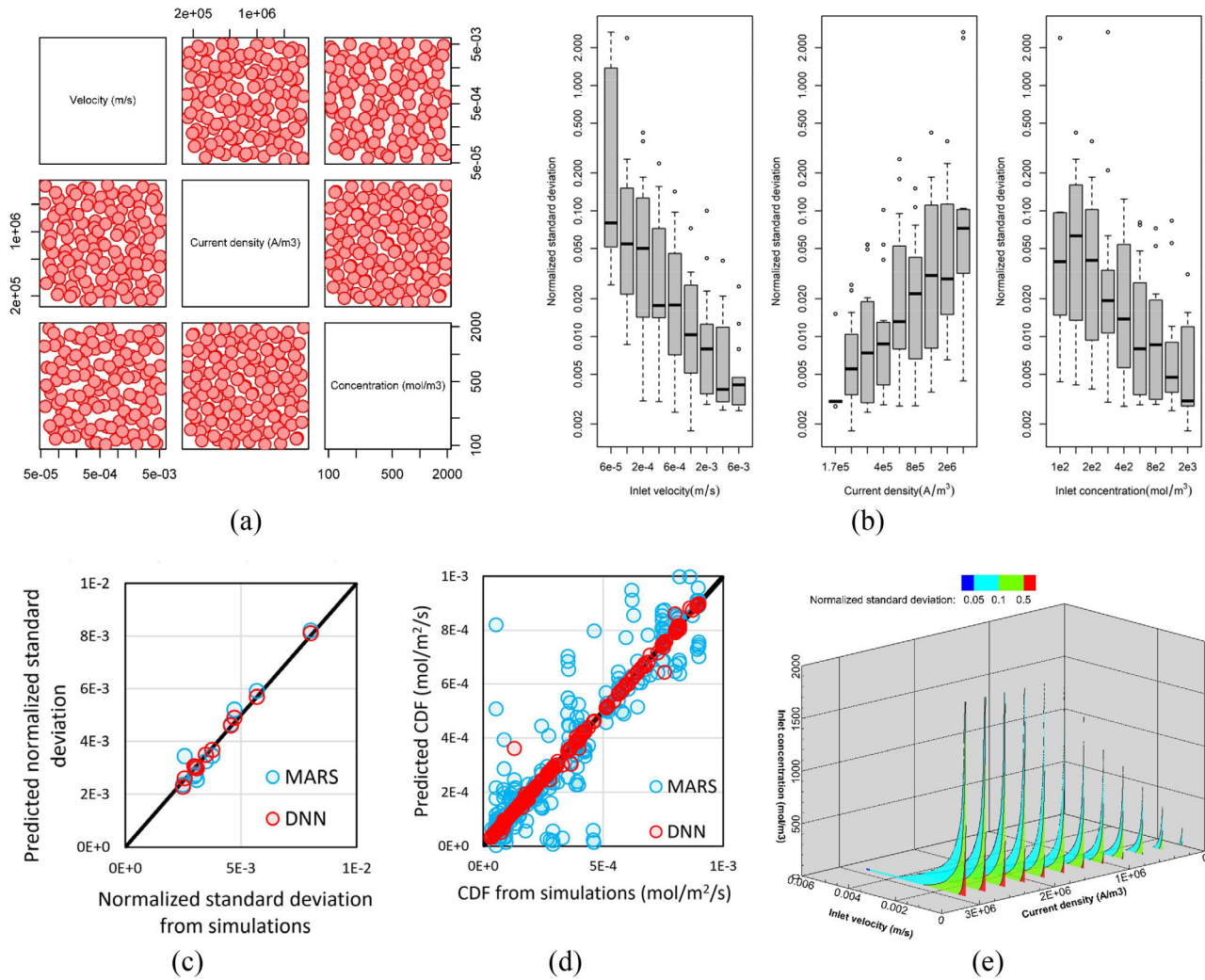
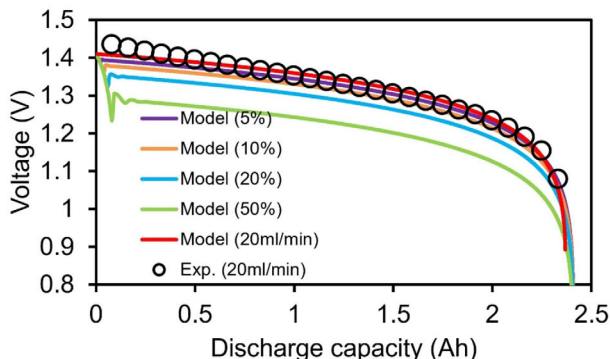


Figure 5. a) 128 QMC samples for inlet velocity, inlet concentration, and electric current density. b) boxplots representing qualitative relationships among the input parameters and the output parameter based on the pore-scale simulation results. c) “one-one” plot to compare the DNN and MARS predicted normalized standard deviations against the true value from simulations for the testing data set. d) “one-one” plot to compare the DNN and MARS predicted CDFs against the true CDFs from simulations for the testing data set. e) Response surface between the input parameters and the output parameter estimated by DNN.

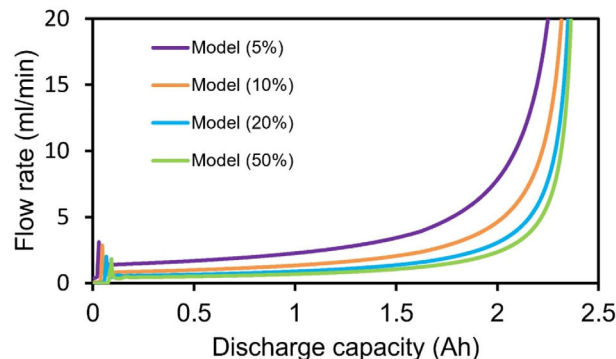
3.3. Device-Scale Estimation by Multi-Scale Framework

The direct pore-scale simulation (Section 4.1) and the DNN prediction (Section 4.2) relate to pore-scale behavior estimations. This section describes how such pore-scale information relates to device-scale models. In our study, we used a half-cell flow battery as an example. As described in Sections 3.3 and 3.5, the positive electrode is simplified into a 1D model that ignores variances in thickness and width. By using the multi-scale framework, σ_r can be estimated at each discretized device-scale grid point at each time step. The combined variance, which represents the reaction uniformity of the whole device, then can be calculated. The optimized inlet speed can be determined to meet the desired surface reaction uniformity (normalized standard deviation of surface reaction rate, $\tilde{\sigma}_r$). Figure 6a shows the discharge voltage varying with discharge capacity. The black circle is the experimental measurement, as described in Section 3.6, with a constant

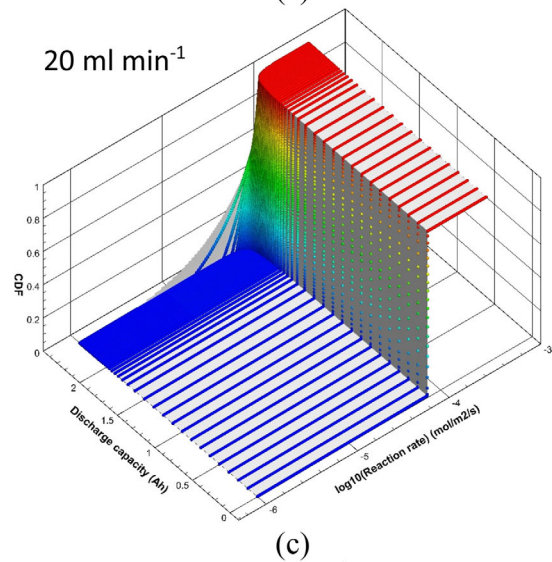
20 mL min⁻¹ flow rate. The red line is the model estimation of the voltage during discharge with the same constant 20 mL min⁻¹ flow rate and other experimental setups. Results from the model match the experimental results fairly well. The other lines in Figure 6a show the model-predicted voltages of optimized time-varying inlet flow rates for different targeted normalized standard deviations of the surface reaction rate ($\tilde{\sigma}_r = 5\%, 10\%, 20\%, \text{ and } 50\%$). With an increase in $\tilde{\sigma}_r$, which means the reaction is more nonuniform on the electrode surface, the discharge voltage slightly decreases. Figure 6b shows the optimized inlet flow rate for different normalized standard deviations of surface reaction rate ($\tilde{\sigma}_r = 5\%, 10\%, 20\%, \text{ and } 50\%$). For $\tilde{\sigma}_r = 5\%$, the battery only requires 10 mL min⁻¹ or less during almost 86% of the charging time. For $\tilde{\sigma}_r = 10\%$, the battery only requires 10 mL min⁻¹ or less during almost 93% of the charging time. Figure 6c-f shows the DNN-predicted CDF evolution with discharge capacity for different flow rates, which provides a direct view of the reaction



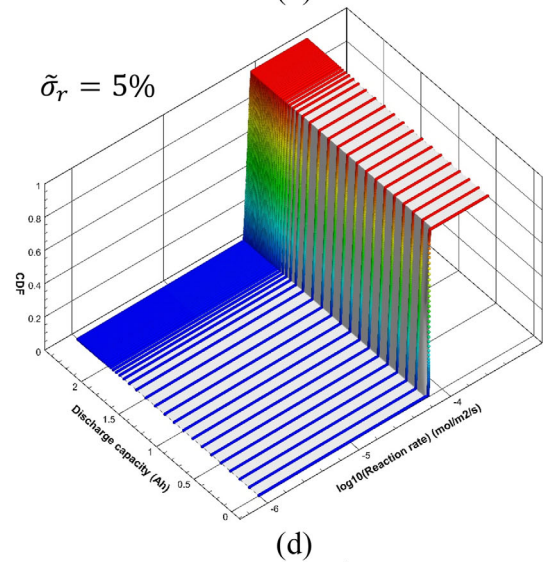
(a)



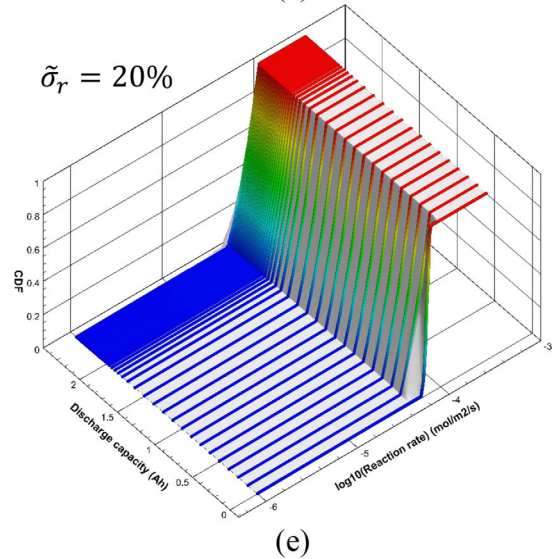
(b)



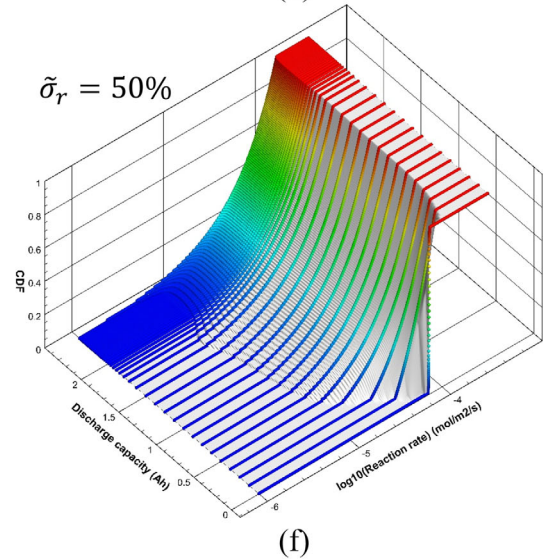
(c)



(d)



(e)



(f)

Figure 6. a) Discharge voltage varying with discharge capacity. b) Optimized flow rate varying with discharge capacity for different target normalized standard deviations of surface reaction rates. c–f) DNN-predicted CDF evolution with discharge capacity for different flow rates. c) Constant 20 mL min^{-1} , d) $\tilde{\sigma}_r = 5\%$; e) $\tilde{\sigma}_r = 20\%$; f) $\tilde{\sigma}_r = 50\%$.

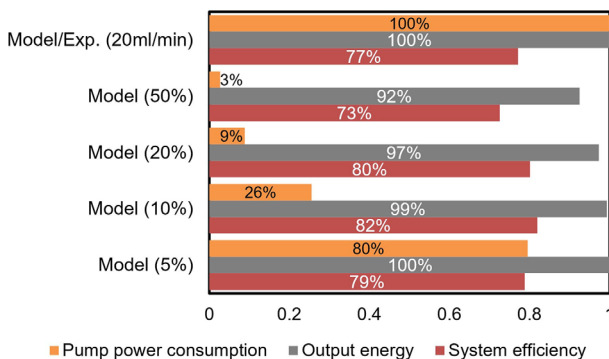


Figure 7. Output energy, pump power consumption, and system efficiency for different targeted σ_r and the constant flow rate (20 mL min^{-1}).

rate distributions. Figure 6c is for the constant flow rate at 20 mL min^{-1} . The very sharp step in CDF from 0 to 1 results from the very small normalized standard deviation of surface reaction rate, which is around 3% and gradually increases to 5% at 2.25 Ah (95% of the total discharge capacity). During the last 5% of the discharge period, the normalized standard deviation of the surface reaction rate rapidly increases to almost 60%. For cases with $\sigma_r = 5\%$ and 20% (Figure 6d,e, respectively), the slope of the transition section in the CDFs is tightly controlled from the beginning to the end of discharge. Because the electrolyte is assumed to fully penetrate into the electrode as the initial condition, the CDF has a very sharp step from 0 to 1 at the first time step. Figure 6f shows CDF evolution for $\sigma_r = 50\%$. Similarly, because of the uniform electrolyte concentration as the initial condition, the CDF also has a sharp step from 0 to 1 at the first time step. The case with $\sigma_r = 50\%$ needs a short discharge period to reach a steady CDF, because the initial uniform electrolyte concentration can lead to a relatively uniform surface reaction where σ_r is smaller than 50%, even with near zero inlet velocity.

By integrating the curves in Figure 6a, the output energy can be calculated. If the output energy at a constant flow rate is 100%, the output energy (defined as r_{output}) for the optimized flow rates for $\sigma_r = 5\%$, 10% , 20% , and 50% is 100%, 99%, 97%, and 92%, respectively, as shown by the gray bars in Figure 7.

It is assumed that the flow-battery pressure drop is mainly caused by the flow in the porous electrode, and ignore the pressure drop in the pipelines. According to Darcy's law, the pressure drop is linear to the flow rate ($\Delta p \propto Q$). The pump power consumption typically is assumed to be linear to the production of pressure drop and flow rate ($P_{\text{pump}} \propto \Delta p Q$), so $P_{\text{pump}} \propto Q^2$. By integrating the curves in Figure 6b with the assumption $P_{\text{pump}} \propto Q^2$, the pump power cost can be roughly compared, as shown by the orange bars in Figure 7. If power consumption at a constant flow rate set at 20 mL min^{-1} is 100%, the optimized flow rate for $\sigma_r = 50\%$ costs only $\approx 3\%$ (defined as r_{pump}) of the constant flow rate (20 mL min^{-1}), $\sigma_r = 20\%$ costs 9% of the power, $\sigma_r = 10\%$ costs 26% of the power, and $\sigma_r = 5\%$ costs 80% of the power. Therefore, the constant flow rate significantly wastes power, thus increasing the overall cost of the flow battery.

The system efficiency of VRFB can be approximately estimated using Equation (15).^[5]

$$SE = \frac{P_{\text{discharge}} \cdot r_{\text{output}} - P_{\text{pump}} \cdot r_{\text{pump}}}{P_{\text{charge}} / r_{\text{output}} + P_{\text{pump}} \cdot r_{\text{pump}}} \quad (15)$$

$P_{\text{discharge}}$ is the discharge power, and P_{charge} is the charge power. If it is assumed that the cell energy efficiency ($\frac{P_{\text{discharge}}}{P_{\text{charge}}}$) is around 0.86 as shown in Figure 3d and the pump power consumption is 5% of the charge power for the constant flow rate (r_{output} and r_{pump} are 1), the system efficiency is 77%. With these assumptions, we estimated the system efficiency for the optimized time-varying flow rate cases, and our estimates are shown as the red bars shown in Figure 7. For the cases with $\sigma_r = 5\%$, 10% , 20% , 50% , the system efficiencies are 79%, 82%, 80%, and 72%, respectively. Therefore, the cases with $\sigma_r = 10\%$ can improve the system efficiency by about 6%, which is the best efficiency achieved in our study.

4. Conclusions and Discussion

This study introduces a multi-scale framework coupled with a DNN ML architecture that can help on advancing our understanding of how pore-scale electrode structure affects device-scale electrochemical reaction uniformity for a flow battery. The pore-scale numerical model is based on the LBE method, which can efficiently simulate flow transport and electrochemical reactions in the pore-scale electrode sample. We used the QMC method to sample 128 pore-scale flow and reaction conditions. Then, we built and trained a DNN based on 128 pore-scale simulations, which provides a quantitative relationship from the battery operating conditions (inlet velocity, current density, inlet concentration) to the surface reaction uniformity standard deviation and CDF for the pore-scale sample. The DNN-estimated surface reaction uniformity is about four times more accurate than the traditional regression model, MARS, as discussed in Section 4.2. In addition, it is very difficult for MARS to predict the valuable full CDF because of its large RMSE, while predictions from the DNN match the true data fairly well. Using the framework and DNN, we were able to upscale information about surface reaction uniformity at the pore level to combined uniformity at the device level. We also validated the information obtained using the framework and DNN against information obtained from experiments. Inlet velocity can be optimized based on this multi-scale framework, and a time-varying inlet velocity can be derived, as shown in Figure 6b for the example flow-battery setup. To keep the relative standard deviation of the surface reaction rate less than 10%, the inlet flow rate needs to be $\leq 10 \text{ mL min}^{-1}$ during almost 93% of the discharging period, which is much lower than the typically used constant 20 mL min^{-1} flow rate. Pump power consumption for a time-varying inlet flow rate for $\sigma_r = 10\%$ is only 26% of the power consumption for constant 20 mL min^{-1} inlet flow rate. The system efficiency for a time-varying inlet flow rate for $\sigma_r = 10\%$ is 82%, which provides $\approx 6\%$ efficiency improvement over the constant flow rate case. DNN-predicted CDF evolution during discharge can provide researchers a direct view of the surface reaction distribution. Additionally, the multi-scale framework can be easily extended to other kinds and designs of flow batteries and different pore-scale electrode structures.

Acknowledgements

The authors J. B., V. M., L. Y., Y. S., and W. W. would like to acknowledge financial support from the U.S. Department of Energy (DOE) Office of Electricity (under Contract No. 57558). The machine learning part in this study was supported by Energy Storage Materials Initiative (ESMI), which is a Laboratory Directed Research and Development Project at Pacific Northwest National Laboratory (PNNL). The ParaFlow software was developed at PNNL by David Rector and Mark Stewart.

Conflict of Interest

The authors declare no conflict of interest.

Keywords

flow batteries, machine learning, multi-scale modeling

Received: August 28, 2019

Revised: October 28, 2019

Published online: November 18, 2019

- [1] J. Noack, N. Roznyatovskaya, T. Herr, P. Fischer, *Angew. Chem., Int. Ed.* **2015**, *54*, 9775.
- [2] A. Z. Weber, M. M. Mench, J. P. Meyers, P. N. Ross, J. T. Gostick, Q. H. Liu, *J. Appl. Electrochem.* **2011**, *41*, 1137.
- [3] G. L. Soloveichik, *Chem. Rev.* **2015**, *115*, 11533.
- [4] M. Park, J. Ryu, W. Wang, J. Cho, *Nat. Rev. Mater.* **2017**, *2*, 16080.
- [5] S. Kim, E. Thomsen, G. Xia, Z. Nie, J. Bao, K. Recknagle, W. Wang, V. Viswanathan, Q. Luo, X. Wei, A. Crawford, G. Coffey, G. Maupin, V. Sprenkle, *J. Power Sources* **2013**, *237*, 300.
- [6] D. You, H. Zhang, J. Chen, *Electrochim. Acta* **2009**, *54*, 6827.
- [7] S. Park, H. J. Lee, H. Lee, H. Kim, *J. Electrochem. Soc.* **2018**, *165*, A3215.
- [8] B. Yang, L. Hooyer-Burkhardt, S. Krishnamoorthy, A. Murali, G. K. S. Prakash, S. R. Narayanan, *J. Electrochem. Soc.* **2016**, *163*, A1442.
- [9] Q. Zheng, X. F. Li, Y. H. Cheng, G. L. Ning, F. Xing, H. M. Zhang, *Appl. Energy* **2014**, *132*, 254.
- [10] Q. Xu, T. S. Zhao, C. Zhang, *Appl. Energy* **2014**, *130*, 139.
- [11] R. L. Fares, J. P. Meyers, M. E. Webber, *Ann. Math. Stat.* **2014**, *113*, 189.
- [12] C. Yin, S. Guo, H. Fang, J. Liu, Y. Li, H. Tang, *Appl. Energy* **2015**, *151*, 237.
- [13] G. Qiu, A. S. Joshi, C. R. Dennison, K. W. Knehr, E. C. Kumbur, Y. Sun, *Electrochim. Acta* **2012**, *64*, 46.
- [14] M. S. Wilson, S. Gottesfeld, *J. Appl. Electrochem.* **1992**, *22*, 1.
- [15] L. R. Jordan, A. K. Shukla, T. Behrsing, N. R. Avery, B. C. Muddle, M. Forsyth, *J. Power Sources* **2000**, *86*, 250.
- [16] D. M. Bernardi, M. W. Verbrugge, *AIChE J.* **1991**, *37*, 1151.
- [17] V. A. Paganin, E. A. Ticianelli, E. R. Gonzalez, *J. Appl. Electrochem.* **1996**, *26*, 297.
- [18] F. Bidault, D. J. L. Brett, P. H. Middleton, N. P. Brandon, *J. Power Sources* **2009**, *187*, 39.
- [19] N. Mahato, A. Banerjee, A. Gupta, S. Omar, K. Balani, *Prog. Mater. Sci.* **2015**, *72*, 141.
- [20] T. Matsumoto, T. Komatsu, K. Arai, T. Yamazaki, M. Kijima, H. Shimizu, Y. Takasawa, J. Nakamura, *Chem. Commun.* **2004**, 840.
- [21] M. Kishimoto, M. Lomberg, E. Ruiz-Trejo, N. P. Brandon, *J. Power Sources* **2014**, *266*, 291.
- [22] H. Al-Fetlawi, A. A. Shah, F. C. Walsh, *Electrochim. Acta* **2010**, *55*, 3192.
- [23] A. A. Shah, H. Al-Fetlawi, F. C. Walsh, *Electrochim. Acta* **2010**, *55*, 1125.
- [24] M. Vynnycky, *Energy* **2010**, *36*, 2242.
- [25] A. A. Shah, M. J. Watt-Smith, F. C. Walsh, *Electrochim. Acta* **2008**, *53*, 8087.
- [26] J. Clement, D. Aaron, M. Mench, *J. Electrochem. Soc.* **2016**, *163*, A5220.
- [27] J. Houser, J. Clement, A. Pezeshki, M. Mench, *J. Power Sources* **2016**, *302*, 369.
- [28] Y. Gandomi, D. Aaron, T. Zawodzinski, M. Mench, *J. Electrochem. Soc.* **2016**, *163*, A5188.
- [29] G. Qiu, C. R. Dennison, K. W. Knehr, E. C. Kumbur, Y. Sun, *J. Power Sources* **2012**, *219*, 223.
- [30] L. Deng, D. Yu, *Found. Trends Signal Process.* **2014**, *7*, 1.
- [31] D. Ciresan, U. Meier, J. Masci, S. Schmidhuber, *Neural Netw.* **2012**, *32*, 333.
- [32] B. Sanchez-Lengeling, A. Aspuru-Guzik, *Science* **2018**, *361*, 360.
- [33] A. Davoudi, Y. Zou, I.C. Camacho, X. Hu, *IEEE Trans. Trans. Electr.* **2016**, *2*, 115.
- [34] X. Hu, S. Li, Y. Yang, *IEEE Trans. Trans. Electr.* **2015**, *2*, 140.
- [35] D. Liu, J. Zhou, D. Pan, Y. Peng, X. Peng, *Measurement* **2015**, *63*, 143.
- [36] J. Bao, W. Xu, P. Bhattacharya, M. Stewart, J. Zhang, W. Pan, *J. Phys. Chem. C* **2015**, *119*, 14851.
- [37] W. Pan, X. Yang, J. Bao, M. Wang, *J. Electrochem. Soc.* **2017**, *164*, E3499.
- [38] P. Trogadas, O. Taiwo, B. Tjaden, T. Neville, P. Yun, J. Parrondo, V. Ramani, M. Coppens, D. Brett, P. Shearing, *Electrochim. Commun.* **2014**, *48*, 155.
- [39] S. Chen, G. D. Doolen, *Annu. Rev. Fluid Mech.* **1998**, *30*, 329.
- [40] R. Benzi, S. Succi, M. Vergassola, *Phys. Rep.* **1992**, *222*, 145.
- [41] D. Yu, R. Mei, L. S. Luo, W. Shyy, *Prog. Aeronaut. Sci.* **2003**, *39*, 329.
- [42] D. R. Noble, S. Chen, J. G. Georgiadis, R. O. Buckius, *Phys. Fluids* **1995**, *7*, 203.
- [43] P. L. Bhatnagar, E. P. Gross, M. Krook, *Phys. Rev.* **1954**, *94*, 511.
- [44] J. Bao, *Doctoral Dissertation*, University of Pittsburgh, Pittsburgh, PA **2010**.
- [45] J. Bao, L. Schaefer, *Appl. Math. Model.* **2013**, *37*, 1860.
- [46] D. Kandhai, A. Koponen, A. Hoekstra, M. Kataja, J. Timonen, P.M.A. Sloot, *J. Comput. Phys.* **1999**, *150*, 482.
- [47] D. E. Eapen, S. R. Choudhury, R. Rengaswamy, *Appl. Surf. Sci.* **2019**, *474*, 262.
- [48] A. Tarantola, *Inverse Problem Theory and Model Parameter Estimation*, Society for Industrial and Applied Mathematics, Philadelphia, PA **2005**.
- [49] Z. Hou, M. Huang, L. R. Leung, G. Lin, D. M. Ricciuto, *J. Geophys. Res.* **2012**, *117*, D15108.
- [50] I. M. Sobol, *USSR Comput. Math. Math. Phys., Engl. Transl.* **1967**, *7*, 86.
- [51] P. Bratley, B. L. Fox, *ACM Trans. Math. Softw.* **1988**, *14*, 88.
- [52] Y. Bengio, A. Courville, P. Vincent, *IEEE Trans. Pattern Anal. Mach. Intell.* **2013**, *35*, 1798.
- [53] M. Abadi, A. Agarwal, P. Barham, E. Brevdo, Z. Chen, C. Citro, G. S. Corrado, A. Davis, J. Dean, M. Devin, S. Ghemawat, I. Goodfellow, A. Harp, G. Irving, M. Isard, R. Jozefowicz, Y. Jia, L. Kaiser, M. Kudlur, J. Levenberg, D. Mané, M. Schuster, R. Monga, S. Moore, D. Murray, C. Olah, J. Shlens, B. Steiner, I. Sutskever, K. Talwar, P. Tucker, V. Vanhoucke, V. Vasudevan, F. Viégas, O. Vinyals, P. Warden, M. Wattenberg, M. Wicke, Y. Yu, X. Zheng, *TensorFlow: Large-Scale Machine Learning on Heterogeneous Systems* **2015**.
- [54] S. Kim, M. Vijayakumar, W. Wang, J. Zhang, B. Chen, Z. Nie, F. Chen, J. Hu, L. Li, Z. Yang, *Phys. Chem. Chem. Phys.* **2011**, *13*, 18186.
- [55] R. McGill, J. Tukey, W. Larsen, *Am. Stat.* **1978**, *32*, 12.
- [56] M. Frigge, D. C. Hoaglin, B. Iglewicz, *Am. Stat.* **1989**, *43*, 50.
- [57] J. H. Friedman, *Ann. Math. Stat.* **1991**, *19*, 1.